Fast-ion transport and toroidal rotation response to externally applied magnetic perturbations at the ASDEX Upgrade tokamak

P. Cano-Megias[1,2], E. Viezzer[2,3], J. Galdon-Quiroga[2,3], L. Sanchis[5], M. Garcia-Munoz[2,3], D.J. Cruz-Zabala[2,3], R.M. McDermott[4], J.F. Rivero-Rodriguez[6], A. Snicker[5], W.A. Suttrop[4], M. Willensdorfer[4] and the ASDEX Upgrade team

[1] *Dept. Energy Engineering, University of Seville, Camino de los Descubrimientos s/n, Isla de la Cartuja, Seville, Spain*
[2] *Centro Nacional de Aceleradores (Universidad de Sevilla, Junta de Andalucia, CSIC), Avda. Thomas A. Edison 7, 41092 Seville, Spain*
[3] *Dept. of Atomic, Molecular and Nuclear Physics, University of Seville, Avda. Reina Mercedes, 41012 Seville, Spain*
[4] *Max Planck Institute for Plasma Physics, Boltzmannstr. 2, 85748 Garching, Germany*
[5] *Dept. of Applied Physics, Aalto University, FI-00076, Aalto, Finland*
[6] *United Kingdom Atomic Energy Authority, Culham Science Centre, Abingdon, OX14 3DB, United Kingdom*

E-mail: pcano1@us.es

Abstract.

This paper studies the effect of 3D magnetic perturbations on fast-ion confinement, and its impact on the toroidal rotation velocity profile. Two low collisionality H-mode experiments carried out at the ASDEX Upgrade tokamak have been analyzed. The two discharges feature different magnetic field helicity (q_{95}), and differences in the velocity-space and level of fast-ion losses are observed. A new analysis technique has been developed that sheds light on the dependencies between fast-ion losses and toroidal rotation, providing for the first time correlation patterns resolved in radius and velocity space of the lost fast-ions. The correlation intensifies towards the plasma edge and is strongly dependent on the orbit topology of the lost fast-ions. The ASCOT orbit following code has been used to characterize the fast-ion resonant transport and beam driven torques, using the vacuum approach and including plasma response. The change of the toroidal canonical momentum, which serves as figure of merit for resonant fast-ion transport, has been calculated with ASCOT. The beam geometry and q_{95} are found to have a strong impact on the fast-ion transport and losses. The fast-ion transport induced by the magnetic perturbations affects the beam driven torques. The effect of the changes of the j×B and collisional torques on plasma rotation is analyzed using the torques simulated by ASCOT and simple momentum balance calculations. For the low $q_{95} = 3.8$ discharge, which benefits from a resonant amplification, we find excellent agreement with the measured variation of the toroidal velocity. For the high $q_{95} = 5.5$ discharge, the inclusion of the plasma response improves the comparison with experimental data with respect to the vacuum estimation, but still some differences with experiments are observed. This suggests that other non-resonant effects could play a role for the determination of the toroidal rotation profile.

1. Introduction

Tokamaks achieve high plasma confinement due to their toroidal field symmetry. In an axisymmetric field particle orbits are closed and transport across flux surfaces is minimized. However, the use of symmetry breaking 3D fields is beneficial for certain applications, e.g. external magnetic perturbations (MP) will be applied as an Edge Localized Modes (ELM) control tool in future fusion devices, such as ITER [1–4].

Symmetry breaking fields can change transport and can lead to a degradation of plasma confinement [5,6]. Non-axisymmetric magnetic perturbations imply that the action of particles is not conserved, such that the turning points of trapped particle orbits drift across flux surfaces and result in enhanced radial transport.

This transport is intrinsically non-ambipolar and can be studied within the neoclassical toroidal viscosity (NTV) theory [5, 7, 8]. The impact of the non-ambipolar fluxes on momentum transport and plasma rotation is widely acknowledged in theory [5, 6, 9, 10] and experiments [11, 12]. In a fluid moment approach, the NTV torque is a viscous force due to a modification of the parallel pressure tensor, which is absent in the case of axi-symmetry [5].

The NTV torque is strongly dependent on plasma collisionality, as collisionality characterizes the role of banana transport on overall transport, and has been described analytically in different collisionality regimes [6, 13, 14]. Kinetic studies have revealed the resonant nature of NTV transport [15] and described the resonance condition for thermal distributions in the case of non-zero $\mathbf{E}\times\mathbf{B}$ rotation [16]. When the resonance condition is not satisfied, transport is minimized as it averages out due to random phase-mixing.

Because of their larger drift-orbit displacements, the number of important resonances increases for energetic particles [17]. The linear resonance condition for energetic particles, in the case of a static perturbation ($\omega_0 = 0$), is given as $n\omega_\phi - p\omega_\theta = 0$, with ω_ϕ and ω_θ being the toroidal and poloidal precession frequencies, n the toroidal mode number and p the bounce harmonic. In addition, the larger orbits facilitate jumps across topological boundaries, which potentially increase radial transport.

In present devices, fast-ions are the dominant momentum source in neutral beam injection (NBI) heated plasmas. Due to their low collision frequency and their relatively long mean free path, fast-ions are especially sensitive to perturbation fields. The fast-ion transport due to externally applied magnetic perturbations has been studied in several tokamaks [18–21]. The existence of a fast-ion Edge Resonant Transport Layer (ERTL) in the presence of externally applied 3D fields has been identified at the ASDEX Upgrade (AUG) tokamak [22]. The resonant interaction at the ERTL is responsible for the radial particle transport leading to fast-ion losses in the presence of perturbative fields, and has been characterized in terms of conservation of toroidal canonical momentum. The transport was identified to satisfy the linear and non-linear resonance conditions depending on the perturbation amplitude.

The redistribution and loss of fast-ions due to MPs can lead to the formation of a radial current, which is compensated by a bulk plasma current to fulfill the ambipolarity condition [23]. The induced current produces a $j_r \times B_\theta$ force that exerts a torque to the plasma and generates a radial electric field, which in turn contributes to the background $\mathbf{E}\times\mathbf{B}$ flows. Because radial forces need to be balanced, changes in $\mathbf{E}\times\mathbf{B}$ flows can lead to changes in plasma rotation and vice versa [24, 25].

The relation between the changes in fast-ion losses and toroidal rotation induced by externally applied 3D fields is studied in this paper, as we analyse the momentum drive and dissipation due to the effect of symmetry breaking on fast-ion transport. To this end, the interplay between these variables is examined in dedicated AUG experiments where MPs are applied, and the dependencies are investigated. The experimental set-up and an overview of the analyzed discharges are described in section 2. The data analysis technique developed in this work is introduced in section 3. The main dependencies of the correlations between fast-ion losses, toroidal plasma rotation and density are presented in section 4. The relation between the correlation analysis results and the resonant interactions responsible for the losses at the ERTL in the presence of 3D fields is assessed in section 5. The impact of fast-ion losses on plasma rotation via momentum balance is studied in section 6. The vacuum as well as the plasma response approach for the magnetic field reconstruction, calculated by the linear VMEC code [26], are considered in both sections 5 and 6. Section 7 gives a summary and outlook.

2. Experiments

2.1. Experimental set-up

The experiments presented in this work were performed at the ASDEX Upgrade (AUG) tokamak. Magnetic perturbations are induced in the AUG tokamak by a set of in-vessel saddle coils, also called B-coils [27]. They sum up to a total of 16 coils which are placed in two arrays (upper and lower row) around the vacuum vessel at the low field side. The B-coils are capable of generating magnetic perturbations (MPs) with toroidal mode numbers $n = 1, 2, 4$ with a maximum normalized perturbation field b_r/B of $\approx 10^{-3}$ for typical -2.5 T

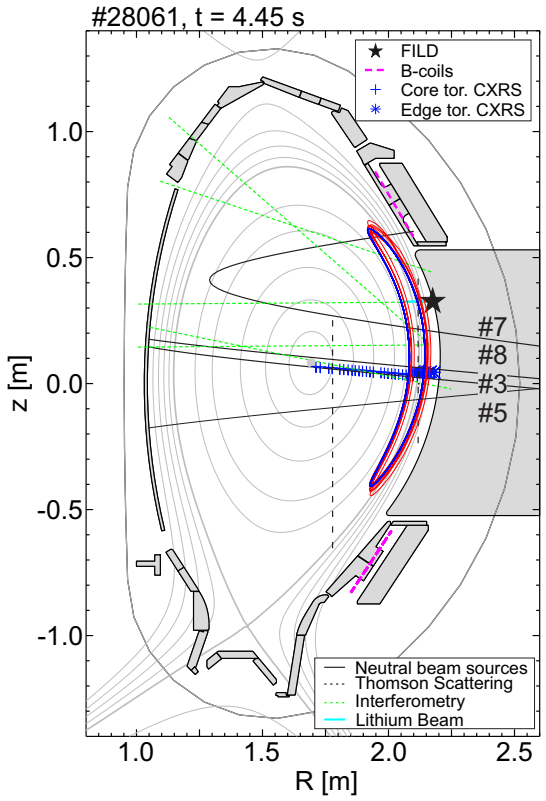

Figure 1. Poloidal cut of ASDEX Upgrade showing the diagnostics used in the study. A trapped orbit in an axisymmetric (blue) and non-axisymmetric magnetic field (red) are shown.

operation. The B-coils are used for ELM control research as they enable the avoidance of type-I ELMs by relaxation of the edge current and pressure gradients [2, 4]. In the discharges presented in this work, static magnetic perturbations with a toroidal mode number $n = 2$ are applied. The phase shift between the upper and lower array of coils is $\Delta\phi = 180°$.

The diagnostics and the geometry of the Neutral Beam Injection (NBI) sources most relevant for this study are shown in figure 1. The guiding-centre trajectory of an NBI trapped fast-ion with a background axisymmetric field is illustrated in blue and with a magnetic perturbation in red. In the case of axisymmetric field, the turning points lie on the same flux surface, while in the non-axisymmetric field, the turning points of the banana orbit move across flux surfaces resulting in radial transport. The energetic ion, which in a background axisymmetric field is well confined, will drift outwards and reach the Fast Ion Loss Detector (FILD) [28] when the magnetic perturbations are applied.

2.2. Experimental observations

Two low collisionality H-mode discharges (#28059, #28061) carried out in the AUG tokamak have been analysed. The discharges follow a similar scheme, but feature differences in the toroidal magnetic field, plasma current, and amplitude of the perturbation field, which are shown in Table 1.

	$\mathbf{I_p}$ **(MA)**	$\mathbf{B_{tor}}$ **(T)**	$\mathbf{I_{B-coils}}$ **(kA)**	$\mathbf{q_{95}}$	$\boldsymbol{\nu^*_{i,ped}}$
#28059	0.8	-2.45	1.0	5.47	0.17-0.6
#28061	0.8	-1.73	1.2	3.80	0.15-0.5

Table 1. Plasma parameters of the analysed discharges: plasma current I_p, toroidal magnetic field B_{tor}, B-coils current $I_{B-coils}$, edge safety factor q_{95} and edge ion collisionality $\nu^*_{i,ped}$. The ion collisionality ($\nu^*_{i,ped}$) is evaluated at $\rho_{pol} = 0.95$ according to [29]. As $\nu^*_{i,ped}$ increases throughout both discharges, the range for $t = [1.5, 4.5]$s is given.

An overview of the discharges is illustrated in figure 2, which shows the time traces of relevant signals for our analysis:

- The current in the B-coils, shown in figures 2(a),(e).
- The electron density, shown in figures 2(b),(f). The electron density is reconstructed within the Integrated Data Analysis (IDA) algorithm based on Bayesian probability theory [30], and combines measurements from different diagnostics and computes the most likely electron profiles constrained by the uncertainties on the data. In these shots, lithium beam, Thomson scattering (TS) and deuterium cyanide interferometry (DCN) measurements are combined.
- The toroidal plasma rotation. The temporal evolution of the impurity toroidal rotation, here measured on C^{6+}, at different radial positions as measured by Charge Exchange Recombination Spectroscopy (CXRS) [31, 32] is shown in figures 2(c),(g). Here, a positive toroidal rotation is in the co-current (and co-beam injection) direction.
- Fast-ion losses. The timetrace of fast-ion losses as measured with FILD1 [28], which is mounted on the sector 8 midplane manipulator (R = 2.176 m, z= 0.33 m, ϕ = 168.8°), is shown in figures 2(d),(h), for discharges #28059 and #28061, respectively.

The spatial and temporal resolutions of the diagnostics is summarized in table 2.

In both discharges three 1500 ms phases follow each other, during which one NBI source is changed (source #3 is always on for diagnostic purposes). The total NBI power (5 MW) and fuelling ($2.3{\cdot}10^{21}$ particles/s) are kept constant within the different phases. In the middle of each NBI phase, MPs are

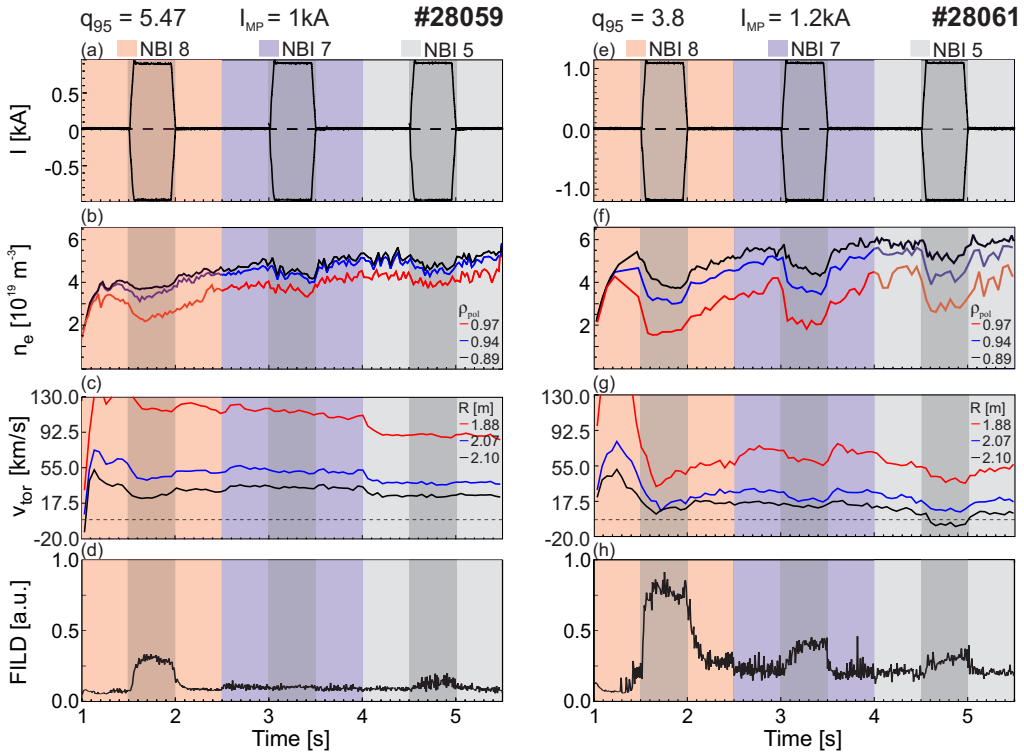

Figure 2. Overview of the H-mode discharges analyzed in this work. The left column shows the time traces of discharge #28059 and the right column of #28061. The time traces of (a,e) the B-coils current, (b,f) electron density (from integrated data analysis), (c,g) toroidal impurity rotation (C^{6+} from Charge Exchange Recombination Spectroscopy) and (d,h) fast-ion losses (as measured by the FILD photo-multiplier tubes) are shown.

Temporal resolution [ms]				
CXRS core	**CXRS edge**	**IDA**	**FILD PMT**	**FILD camera**
3.5	2.3	1	0.001	20
Spatial resolution [mm]				
CXRS core	**CXRS edge**	**TS core**	**TS edge**	**Lithium beam**
20	3	25	3	5

Table 2. Spatial and temporal resolution of the diagnostics used in the analysis. [31, 33, 34]

applied for 500 ms, which is indicated with a darker shaded phase. The different NBI phases are indicated with colours (beam source #8 with a radial on-axis geometry in red, beam source #7 with a tangential off-axis geometry in blue and beam source #5 with a radial on-axis geometry in gray). The full energy component of beam source #3 is 60 keV, while for beam sources #5, #7 and #8 it is 93 keV. This experimental set-up allows us to study the effect of MPs when different NBI sources are applied. Note that because the plasma is not yet stationary before the first MP phase in discharge #28061, this phase will be excluded from the analysis. A clear impact of the MP on plasma profiles is observed in most phases, i.e. density pump-out [35–38] and rotation braking [39–41]. The response of the fast-ion losses is also clearly correlated with the application of MPs [18, 19].

We also observe important differences regarding how strongly the plasma reacts to the externally applied magnetic perturbation when we compare the high and low q_{95} discharges and the three NBI phases. Please note that the density steadily increases throughout both discharges, providing a transition from lower (phase 1) to higher (phase 3) collisionality. This can lead to a better shielding of the MP with the higher collisionality, as discussed in section 2.3.
The density pump-out phenomenon is clearly observed, at about 10% and 25% in the pedestal region for shots #28059 and #28061, respectively, as shown in figures 2(b),(f). The density pump-out is mitigated as the discharges progress, and collisionality increases. It is accompanied by marginal ELM mitigation, i.e. the ELM frequency increases and the energy loss of an individual ELM is reduced [42]. The electron and ion temperatures are not significantly affected by the application of the MPs in these discharges (not shown here). Regarding the plasma confinement, the stored energy and energy confinement time decrease around 15% in the MP phases compared to the axisymmetric phases in #28061, while there is no noticeable change in discharge #28059. The degradation of the confinement is connected to the density pump-out [35, 41].

During the application of MPs, the plasma co-

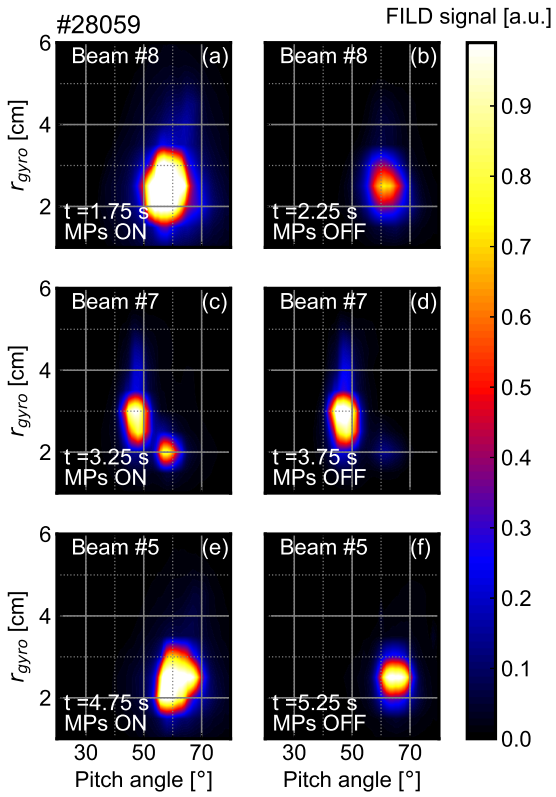

Figure 3. Overview of velocity-space resolved fast-ion losses for a high q_{95} discharge when MPs are on (left) and off (right).

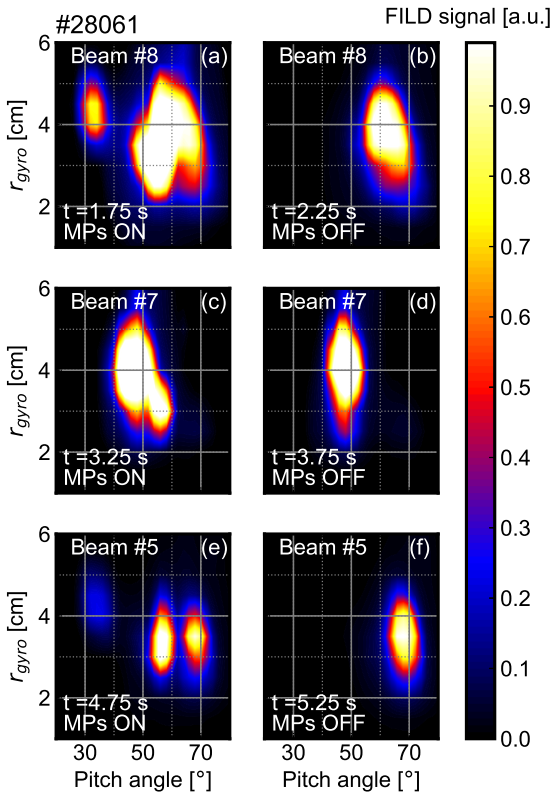

Figure 4. Overview of velocity-space resolved fast-ion losses for a low q_{95} discharge when MPs are on (left) and off (right).

I_p toroidal rotation is reduced over the full plasma radius. This is clearly visible in the second and third phases of the low q_{95} discharge, as shown in figures 2(g). At high q_{95}, the rotation changes only in the low collisionality phase (phase 1), as can be seen in 2(c). In addition, during the last MP phase of discharge #28061, impurity acceleration in the counter-I_p direction is observed at the plasma edge [43], shown in black in figure 2(g). This is evidence for a change in the torque (reduction of co-I_p torque or increase of counter-I_p torque), opposed to rotation braking/dissipation. This is not seen in discharge #28059, where the toroidal rotation is always above zero.

Figures 2(d),(h) show the fast-ion losses integrated in velocity space (the signal from all photo-multiplier tubes is summed up). Interestingly, the fast-ion losses are significantly different from one phase to another depending on the NBI source. This can be seen in both the magnitude of the losses and the response times, which are seen to differ from radial (first and third phase) to tangential (second phase) injection in figure 2(h). On the one hand, the MP-induced fast-ion losses increase by a factor of up to 5 compared to the NBI prompt loss level without MPs in the lowest collisionality phases, as can be seen in figure 2(h). On the other hand, no change in the fast-ion loss level is observed in the second phase (tangential off-axis beam) in the high q_{95} discharge. Please note that the absence of a change in the fast-ion loss level does not imply that no fast-ion losses are measured, as there is some level of fast-ion losses in the absence of any MPs. Figures 3 and 4 give an overview of the velocity-space resolved fast-ion losses as measured by the FILD CCD camera during (left) and before (right) the application of MPs for the high and low q_{95} cases, respectively, as a function of gyroradius (r_{gyro}, or energy) and pitch angle (Λ, where $\Lambda = \arccos\left(v_{\parallel}/v_{tot}\right)$). Generally, the fast-ion losses increase with the application of MPs [18, 19]. MPs produce losses of fast-ions that would be well confined in the absence of any perturbations, e.g. the region around $\Lambda \approx 58°$ and $r_{gyro} \approx 3.2$ cm becomes visible when MPs are applied in the third phase of the low q_{95} case (see Figure 4(e)). Interestingly, we observe that the measured fast-ion losses can also be mitigated for certain values of r_{gyro} and Λ. For instance, fast-ion losses for $\Lambda > 65°$ and $\Lambda > 60°$ are mitigated in the third phase of discharges #28059 and #28061,

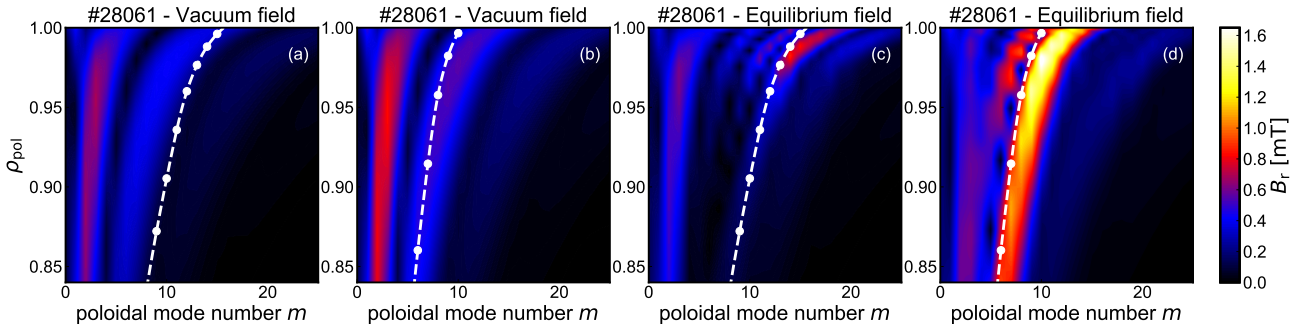

Figure 5. The poloidal mode spectra of the external MP-field n = 2 in (a-b) the vacuum field approximation, and (c-d) including plasma response using VMEC for (a,c) #28059 and for (b,d) #28061 . The pitch aligned components and the rational surfaces are shown as dashed lines and white circles, respectively.

respectively (figures 3(e,f) and 4(e,f)), as well as for $\Lambda < 50°$ for the high q_{95} case (figures 3(c,d)). The differences between the phases can be attributed to the fast-ion transport dependence on the perturbation field and the fast-ion space populated by a given NBI. Both points will be discussed in further detail in section 5.

It is important to note that magnetic perturbations act on the multi-transport channels through different physics mechanisms. For example, non-resonant and resonant momentum transport, affect the toroidal rotation profile, while formation of edge stochastic layers may be a key mechanism to determine particle transport (density pump-out). However, the effect of MPs on the particle and momentum transport channels may not be completely independent. For this reason, the density pump-out has been considered for the calculations of the toroidal rotation changes induced by MPs presented in section 6.

The different effects of the perturbation on the parameters of interest (fast-ion losses, plasma toroidal rotation and plasma density) reported in this section might be due to the differences in q_{95} and perturbation amplitude. These, in turn, can have an impact on the plasma response.

2.3. Magnetic field reconstruction

In this work, both the vacuum approach and the plasma response fields have been used for the estimation of fast-ion transport and the NBI driven torques. Plasma response is a very active research topic, and several works have shown the importance of considering the plasma response currents when a 3D field perturbation is applied [1, 44–52]. When an external perturbation field is applied to the plasma, the plasma can react amplifying, suppressing, or modifying the perturbation field. Response currents are often driven at the rational surfaces (those meeting the $q = m/n$ requirement, where m is the poloidal mode number and n the toroidal mode number), which partially or fully shield the resonant field components. The perturbation field can also be amplified by the plasma. The ideal kink response produces the excitation of non-resonant components, and possibly of resonant components via poloidal mode coupling. Previous works showed that the safety factor (or q_{95}), the poloidal spectrum of the perturbation, the plasma density/collisionality and the amplitude of the perturbation field are important players to explain the plasma response to MPs [35, 36, 41, 46]. The differences between the two discharges with respect to these parameters is addressed below.

The poloidal spectrum of the perturbation in vacuum is shown in figures 5(a-b). Despite the fact that the two equilibria feature different q_{95}, no major differences can be highlighted. Note that the poloidal spectrum of the perturbation changes quite substantially depending on the q_{95} when the plasma response is included, as shown in figure 5(c-d). In both cases the plasma response is shielding the field aligned component. However, we observe that for the low q_{95} discharge (#28061), the plasma response amplification of the perturbation is quite strong, while in the high q_{95} discharge (#28059) there is almost no amplification. The amplification/shielding of the perturbation is consistent with the observation of phenomena such as density pump-out, fast-ion losses and rotation braking [18, 19, 35, 41]: i.e. in the low q_{95} discharge, where we get an amplification of the perturbation, the changes of toroidal rotation, electron density and fast-ion losses due to the application of MPs are larger. Note that the differential phase ($\Delta\phi$) that maximizes plasma response depends on q_{95} [46], such that strong plasma response could also be attained for the high q_{95} discharge at a different $\Delta\phi$.

While there are differences in the collisionality between the two discharges, both discharges are in the banana regime, $\nu_i^* < 1$, for all $\rho_{pol} < 0.95$, where the collisionality has been calculated with equation 9 in [29]. Thus, we do not expect that the changes

in the collisionality are responsible for the striking differences between the two discharges. The changes in the collisionality throughout discharge #28059 likely explain the fact that the perturbation is effective in the first MP phase, at the lowest density/collisionality, while the perturbation is effectively shielded in the later phases of this discharge. This is also seen as the density pump-out becomes weaker throughout both discharges. A slight but steady increase in the density (and collisionality) across the discharges could provide an explanation, as they are related to a better shielding against MPs penetration [41]. Note that a higher relative perturbation (i.e. I_{Bcoils}/B_{tor}) is applied in #28061 compared to #28059, which might also contribute to a larger overall impact of the applied perturbation on the plasma parameters. In the low q_{95} discharge and in the low-collisionality phase of the high q_{95} case the magnetic perturbations induce (1) fast-ion resonant transport, which leads to their redistribution and loss, and in turn influences the fast-ion $j \times B$ torque and (2) density pump-out or confinement loss, which leads to changes in the beam deposition and beam collisional torque, and on the momentum confinement time. In the next sections, we present analysis and modeling tools that allow us to investigate the relation between the response of the three analyzed quantities, i.e. fast-ion losses, plasma density and plasma toroidal rotation, to the MPs and to address the important differences between the high and low q_{95} experiments.

3. Correlation technique for data analysis

The coupled temporal evolution of the signals of interest (i.e. electron density, toroidal rotation and fast-ion losses) has been studied using the linear Pearson coefficient as a figure of merit. It is defined as:

$$C_{x,y} = \sigma_x \sigma_y / \sigma_{xy}$$

where σ_x represents the standard deviation of variable X, σ_y the standard deviation of variable Y and σ_{xy} is the covariance of variables X and Y. The mapping of the diagnostics has been done with a 2D equilibrium reconstruction. The CXRS measurements from the core and edge systems (with a resolution of 3.5 and 2.3 ms, respectively), which are performed at fixed radial positions, are combined and mapped onto the magnetic equilibrium (reconstructed with a time resolution of 1 ms) to obtain profiles along the ρ_{pol} coordinate. The faster measurements have been down-sampled to the time base of the core CXRS diagnostic prior to the calculation of the correlation to make the time bases of the different diagnostics compatible. In this section, the slower timebase is the core CXRS measurements, while in section 4 the slower timebase is that of the FILD CCD camera (see table 2). The correlation between the temporal evolution of a pair of signals has been calculated for the full discharge to quantify the impact (if any) of the magnetic perturbations on the signals. For this purpose, the correlation has been calculated in time windows of 300 ms (t_{window}). The time window is shifted 30 ms (t_{lag}) and the correlation is calculated for the subsequent time window. This time lag was introduced to resolve the temporal evolution of the correlation between a pair of signals. The method is illustrated for clarity in figure 6. A sensitivity scan was carried out to select appropriate values for the parameters t_{window} and t_{lag}, such that the changes in the correlation can be resolved with detail in time while the noise is kept under an acceptable level. The noise in the calculation of the correlation is reduced by taking larger sample sizes [53]. To have statistically significant correlations, a minimum sample size of 50 measurements has been considered. This provides a minimum 175 ms t_{window} duration (taking into account the longest time resolution of the core CXRS system), while the maximum t_{window} duration was limited by the length of the MP phases (500 ms).

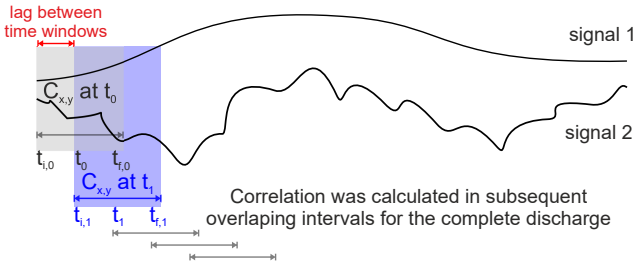

Figure 6. Technique to analyze the variation in the correlation coefficient between a pair of signals as a function of time. The parameters t_{window} and t_{lag} are illustrated.

The correlation coefficient ranges between 1 and -1, such that values close to |1| indicate a strong coupled evolution over time, while values close to 0 indicate the temporal evolution is decoupled. The sign determines if the evolution of the signals follows the same behaviour i.e. when both increase/decrease in time the sign of the correlation is positive, or an opposite behaviour, i.e. when one signal is increasing over time and the other is decreasing, the sign of the correlation is negative.

The correlation between the toroidal rotation and the fast-ion losses integrated over the whole velocity space ($C_{vtor,FIL}$) is presented in figures 7(a),(b) for discharges #28059 and #28061, respectively. The dashed lines indicate when the B-coils are switched on and off. The correlation is clearly modulated by the MPs for all phases in the low q_{95} discharge (#28061) and for the first phase of the high q_{95} (#28059),

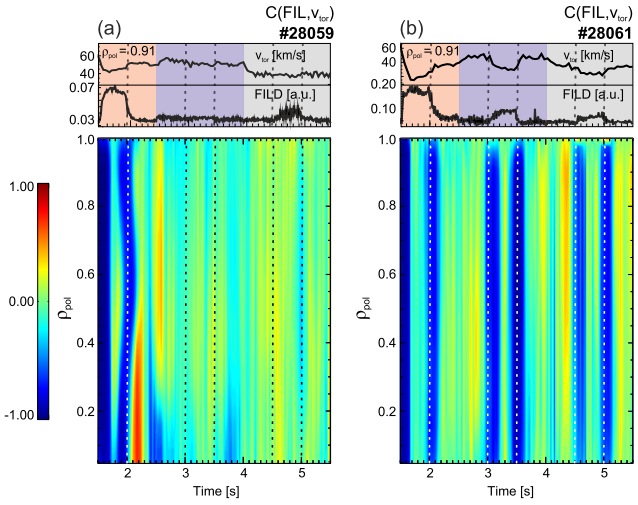

Figure 7. Correlation maps between fast-ion losses and toroidal rotation as a function of time and ρ_{pol} for discharges (a) #28059 and (b) #28061. The switching on and off of the B-coils is indicated with dashed lines. The temporal evolution of toroidal rotation and fast-ion losses are given for reference on the top plots. The changes in the NBI beams are indicated using different colours in the background (red, blue, gray).

consistently with the description given in section 2.1. In these cases, when the B-coils are switched on, the fast-ion losses increase and the rotation decreases, while when they are switched off, the fast-ion losses decrease and the rotation increases, leading to negative correlation in both cases. When comparing figures 7(a) and 7(b), we observe that the correlation modulation is stronger for discharge #28061 than for #28059. Since the two discharges have a different q_{95} (see Table 1), the poloidal spectrum of the perturbation is different (although the differential phase of the applied spectrum is the same $\Delta\phi = 180°$). This plays an important role, as the poloidal spectrum of the perturbation can have a strong impact on the plasma response [35, 41]. In addition, a stronger impact of the MPs on the correlation could be due to the higher relative perturbation (I_{Bcoils}/B_{tor} ratio) for discharge #28061 (as already mentioned in section 2.2), i.e. the I_{Bcoils}/B_{tor} ratio in shot #28061 is 1.7 times the ratio in shot #28059 [54].

Figures 7(a-b) complement figure 2, as they show that the negative correlation structures extend mostly for all ρ_{pol}. These correlation maps give a general overview of the spatial and temporal evolution of the variables. The steady phase during the application of MPs shows up as intervals with low correlation values (coloured in green/turquoise/yellow) in between the high negative correlation structures. The correlation between fast-ion losses and density is similar to the correlation between fast-ion losses and toroidal rotation shown in figures 7. The correlation between toroidal rotation and electron density shows a similar pattern but in this case has a positive sign, as both variables decrease due to the application of the MP.

The correlation structures are generally homogeneous for all radial positions, as density and rotation profiles undergo a general drop due to the MPs. These figures are not presented here for simplicity.

4. Main parametric dependencies of the correlation

In this section, the signal of the FILD CCD camera is used to analyze the fast-ion losses in terms of pitch angle (Λ) and gyroradius (r_{gyro}). The correlation coefficient was calculated between the temporal evolution of electron density or toroidal rotation for all radial positions and the temporal evolution of fast-ion losses for different pairs of Λ and r_{gyro} during an MP phase. The signals have been downsampled to the time base of the FILD camera (see table 2). Using the FILD signal from the CCD camera allows us to determine whether or not the whole velocity space of fast-ions follows a similar response to the MP. In this case, a grid with a resolution of 2° in pitch angle and 0.5 cm in gyroradius has been defined, and the signal from a range of pitch angle $[\Lambda-1, \Lambda+1]°$ and gyroradius $[r_{gyro}-0.25, r_{gyro}+0.25]$ cm has been grouped together. The correlation has been calculated between electron density/toroidal rotation and fast-ion losses in a specific range of gyroradius and pitch angle.

Figure 8(a) shows the correlation map between fast-ion losses and toroidal rotation as a function of pitch angle and gyroradius at a fixed radial position ($\rho_{pol} = 0.99$). This correlation map allow us to identify regions with mitigated/enhanced losses.

By comparing figure 8(a) to figures 4(e-f), the regions with high absolute correlation values can be connected with the regions in which fast-ion losses are produced. At $\rho_{pol} = 0.99$, the toroidal rotation decreases in time: this means that the correlation is positive when the FILD signal decreases and negative when the FILD signal increases. The correlation map for electron density and fast-ion losses is similar to 8(a), and the maps show similar structures when calculated for different radial locations.

Note that towards the core, the density and toroidal rotation respond similarly but less intensely to MPs (i.e. both decrease), so that deeper inside the plasma the pattern seen in the correlation map for rotation and density remains similar to the one obtained for electron density at $\rho_{pol} = 0.99$, but absolute values of the correlation are lower. There is an abrupt change in the correlation coefficient for a given pitch angle, as can be seen in figures 8(a) and (b). Around pitch angle $55 - 66°$ the correlation coefficient changes from -0.90 to +0.90. This is related

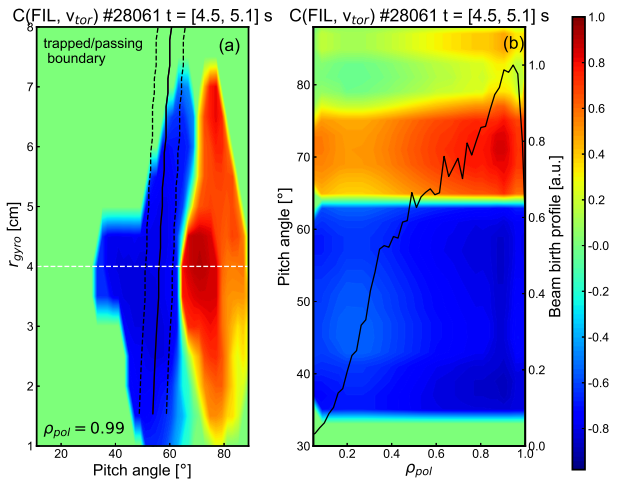

Figure 8. Correlation between fast-ion losses and toroidal rotation as a function of (a) pitch angle (Λ) and gyroradius (r_{gyro}) of the fast-ions for gyro-radius ($\rho_{pol} = 0.99$) and (b) ρ_{pol} and pitch angle for the gyroradius that corresponds to the first energy component of 93 keV. The trapped/passing boundary is shown in a black solid line in (a). The dashed lines represent a shift of $\pm 5°$ that corresponds to the uncertainty of the FILD detector and width of the trapped/passing boundary. The beam #5 birth profile is shown in black in (b) for reference. The deposition peaks when the correlation maximizes.

to the enhancement and mitigation of fast-ion losses depending on the velocity-space.

Interestingly, this abrupt change coincides with the trapped/passing boundary (shown with a black solid line in figure 8(a)), which suggests that the loss pattern is strongly dependent on the topology of the orbit. The solid dashed lines represent a shift of $\pm 5°$ that corresponds to the uncertainty of the FILD detector and width of the trapped/passing boundary. In this case, MPs enhance the losses of passing particles, with pitch angle below $\approx 55 - 60°$, while losses at pitch angle $\geq 60°$ are reduced. A similar pattern is seen for the same phase (third phase, radial NBI injection) in discharge #28059, and in the first phase of both discharges (also radial NBI injection). This pattern is not observed for all phases. For instance, for the second phase in discharge #28059 an opposite effect is seen, as losses are mitigated for pitch angles around [40,50]° and enhanced for pitch angles [60,70]°(which can be deduced from figures 3(c-d)). In this case the correlation is low, in agreement with the fact that the response of toroidal rotation and electron density to the MPs is weak in that phase.

Figure 8(b) shows changes in the correlation between toroidal rotation and fast-ion losses as a function of pitch angle and radial position for a fixed gyroradius (a cut-through along the white dashed line indicated in figure 8(a), now varying the radial coordinate given by ρ_{pol}). . The correlations are calculated for the measured fast-ion losses with gyroradii ranging from 3.5 to 4 cm, corresponding to the first energy component of the NBI injected fast-ions of 93 keV. Figure 8(b) shows that the correlation structures extend for all radial positions and intensify towards the plasma edge (from ρ_{pol} around 0.87 to 0.98). This corresponds to the region where NBI fast-ions are born and suggests that the largest effects of fast-ion losses on rotation are at the edge, in agreement with the fact that in this case fast-ions striking on FILD are edge particles exploring the pedestal region. The NBI birth profile for source #5 is shown for reference, which indeed peaks in the pedestal region.

5. Relation to Edge Resonant Transport Layer

In this section, we relate the strong dependence of the correlation pattern with the trapped/passing boundary (as introduced in section 4, see figure 8(a,b)) with the resonances involved in the fast-ion transport around the trapped/passing boundary predicted by the Edge Resonant Transport Layer (ERTL) model [22].

The ERTL is a region of linear and non-linear radial transport of fast ions that resonate with the externally imposed magnetic perturbation. The ERTL is localized at the plasma edge and has been characterized in terms of conservation of constants of motion by calculating the temporal variation of the toroidal canonical momentum (P_ϕ) [22] with the Monte Carlo orbit following code ASCOT [55]. In perfect toroidal symmetry, P_ϕ, which is defined as

$$P_\phi = mRv_\phi - Ze\psi \quad (1)$$

is conserved. Here m is the ion mass, R is the major radius, v_ϕ is the toroidal velocity, Ze is the ion charge and ψ the poloidal magnetic flux. In the presence of non-axisymmetric fields P_ϕ is no longer a constant of motion and radial drift of particles can occur. From equation 1 one can extract that an increase in P_ϕ leads to inward transport while a decrease leads to outward transport.

In [22], ASCOT was used to characterize the impact of the poloidal spectra of the perturbation, collisions and radial electric field on the ERTL topology using the vacuum approach and including plasma response. It was found that particles around the trapped/passing boundary, which is a region with very high resonance density, might experience significant radial transport due to resonance overlap.

As previously mentioned in section 2, important differences are seen regarding the impact of MPs on the fast-ion losses when different neutral beam injectors are used. This suggests that the interactions between the applied 3D perturbation field and the NBI phase space distribution at birth could play an important role. To this end, we have used ASCOT to study the resonant

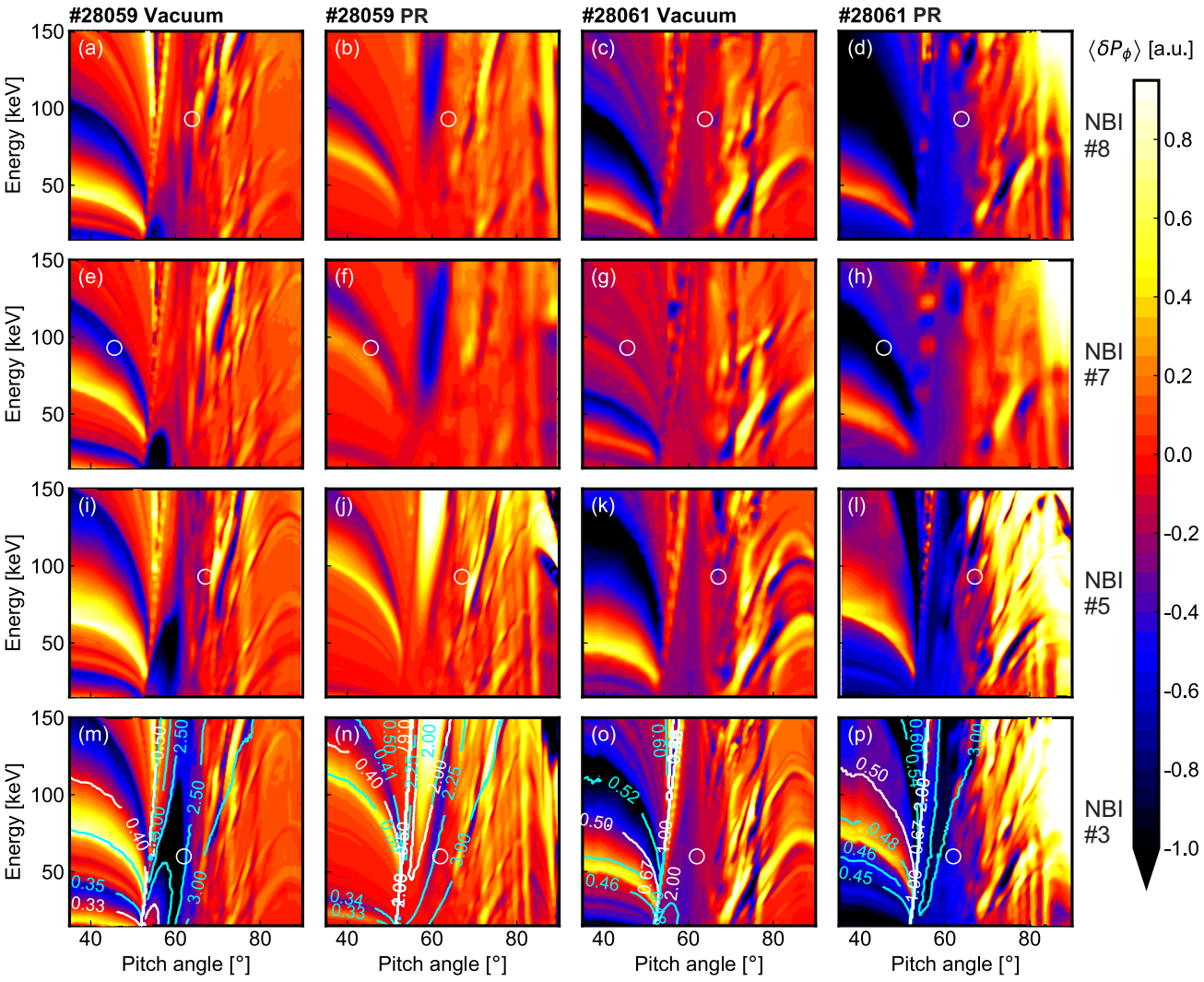

Figure 9. Averaged temporal variation of the toroidal canonical momentum ($\langle \delta P_\phi \rangle$) calculated by ASCOT as a function of the energy and pitch angle of the beam fast-ions with the initial conditions characteristic of each NBI source. The characteristic pitch at birth and full energy is indicated with a white circle for each beam. The different rows represent each of the 4 NBI sources (sources #8, #7 and #5 used in each phase, and source #3 which was always on for diagnostic purposes). Each column refers to a magnetic equilibrium, where the first and second column use the vacuum and plasma response (PR) high q_{95} (#28059) reconstruction, respectively, and the third and fourth column show the vacuum and plasma response low q_{95} (#28061) case. The linear (white) and non-linear (cyan) geometrical resonances $\omega_{pol}/\omega_{tor}$ are shown for source #3 as example cases. The geometrical resonances explain the variations in $\langle \delta P_\phi \rangle$, indicating transport is resonant.

transport of NBI born fast-ions using $\langle \delta P_\phi \rangle$ as a figure of merit. Figure 9 shows the simulated $\langle \delta P_\phi \rangle$ map as a function of the energy and pitch angle of beam fast-ions in the high (columns 1, figures 9(a,e,i,m), and 2, figures 9(b,f,j,n)) and low (column 3, figures 9(c,g,k,o), and column 4, figures 9(d,h,l,p)) q_{95} equilibria. An artificial ensemble of test particles are started at the peak birth location in real space (R, z and ϕ) of each NBI source (sources #8, #7 and #5 used in the experiment, as well as source #3 which was always on for diagnostic purposes, from top to bottom row). The markers are followed forwards in time, scanning their pitch angle and energy. To calculate $\langle \delta P_\phi \rangle$, the particle trajectories have been calculated in full orbit simulations using a full 3D wall geometry and magnetic field, which includes the externally imposed 3D fields in vacuum approach (shown in the first and third columns of figure 9) and including the plasma response (PR) as calculated by the VMEC code [26] (shown in the second and fourth columns of figure 9). The characteristic pitch and full energy component of each beam is shown with a white circle. Please note that the initial conditions of the markers correspond to the birth fast-ion conditions, however, fast ions may experience radial transport due to the interaction with the perturbed fields along their full orbits.

In general, it is interesting to note that in the low q_{95} equilibrium, including the plasma response enhances both inward (for $\Lambda > 80°$, there is an increase of a factor of 7) and outward (for $55° < \Lambda < 65°$, an increase of a factor of 3) radial fast-ion transport. This can be noticed by comparing third (vacuum) and fourth (plasma response) rows for all beams. When we focus on the overlap of the $\langle \delta P_\phi \rangle$ changes with the birth pitch angle and energy of each beam (white circle), we find the clearest overlap for source #7. For its birth conditions (white circle), the outward (blue) transport is strongly enhanced when including plasma response, as can be seen in figure 9(h), compared to the vacuum case (figure 9(g)). For beam sources #3 and #8 outward transport is also enhanced at the birth conditions. These observations are in line with the experiment, as we observe that the fast-ion losses increase in all phases when applying the MPs. The enhanced fast-ion radial transport, which is predicted when including the plasma response, can potentially lead to this increased level of fast-ion losses as measured with the FILD detector. While source #5 birth conditions do not coincide with strong variations of $\langle \delta P_\phi \rangle$, we do observe that $\langle \delta P_\phi \rangle > 0$ for the $\Lambda \gtrsim 65°$ (leading to inward transport, therefore mitigated losses) and $\langle \delta P_\phi \rangle < 0$ for $\Lambda \lesssim 65°$ (leading to outward transport, therefore enhanced losses), which is indeed in qualitative agreement with the experimental observation, as can be seen by comparing figures 4(e,f).

For the high q_{95} equilibrium (columns 1 and 2 of figure 9), we observe in general the opposite effect, as including the plasma response results in a reduction of the resonant structures, which would lead to a reduction of fast-ion resonant radial transport. For example, outward radial fast-ion transport for source #3 would be expected for discharge #28059, when estimating radial transport using vacuum fields, as seen in figure 9(m). The inclusion of the plasma response in the high q_{95} case results in a mitigation of such transport, as shown in figure 9(n). This can be noted as the reduction of the outward transport structure, in blue, at $\Lambda = [55, 65]°$ in figure 9(n) compared to figure 9(m). We observe a similar effect for beam source #7, as including plasma response results in a mitigation of the outward radial transport (figure 9(e)) compared to the vacuum case (figure 9(f)). This is in line with the experimental observations, as in this phase, we do not observe an enhancement of fast-ion losses due to the MPs. For source #8, for which we see the largest increase in fast-ion losses, we observe that the birth conditions do not coincide with regions of outward transport in vacuum, as shown in figure 9(a). However, a region of outward transport emerges at pitch angle of 60° (figure 9(b)) when plasma response is included, which could potentially explain the enhanced

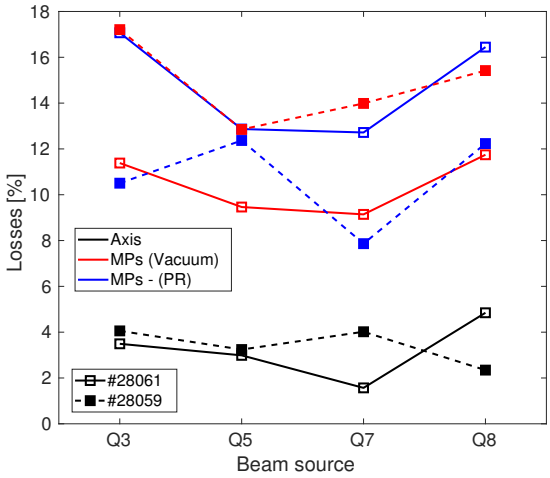

Figure 10. Total fast-ion losses upon thermalization as a function of the beam source for different magnetic equilibrium (colours) and the high (filled marker, dashed line) and low (empty marker, solid line) q_{95}.

experimental losses. For beam source #5 we obtain lower agreement with the experiment, as we would expect some inward radial transport from figure 9(j) while in the experiment we observe a small increase in fast-ion losses.

These simulation results are in line with the experimental observations reported in section 2, as we noted that the fast-ion losses were amplified in the low q_{95} discharge while the effect was smaller in the high q_{95} discharge. The ERTL can provide an explanation for the abrupt change in the correlation pattern with the pitch angle (shown in section 4) as the fast-ion transport due to MPs is resonant and thus, strongly dependent on the ion orbit topology.

To address the fact that these calculations are limited to the birth conditions of the fast-ions, additional simulations have been carried out to estimate the total losses to the wall, upon thermalization of the beam fast-ions. This is also relevant, as FILD detectors are limited to a poloidal and toroidal location and may not be representative of the total losses when 3D non-axisymmetric fields are applied. Figure 10 shows an overview of the total losses to the wall predicted with ASCOT for the high and low q_{95} discharges the using axisymmetric equilibrium, MP fields in vacuum and MP fields including plasma response. When MPs are included (in red for vacuum approximation and blue for plasma response), the losses increase by a factor of 3-4 for all beams and both discharges compared to the axisymmetric case (in black). For the low q_{95} discharge including the plasma response correction (solid blue) results in enhanced fast-ion losses compared to the vacuum case (solid red), while for the high q_{95} case the plasma response fields

(dashed blue) lead to a mitigated loss level (dashed red). This trend is consistent with the results reported from the $\langle \delta P_\phi \rangle$ analysis, and highlights the importance of considering the effects of plasma response, as it can not only mitigate the losses by perturbation shielding, but also enhance them.

6. The connection between fast-ion losses and rotation via momentum balance

Momentum from high-energy neutral beams is transferred to the plasma by a combination of collisional and electromagnetic mechanisms. Upon ionization of the beam neutrals, the large radial excursions of fast-ions with respect to their birth location together with a radial density gradient lead to the formation of a plasma current which exerts a torque on the plasma. Therefore, the $j \times B$ force associated with this current can be expressed in terms of the radial fast-ion current. The $j \times B$ and collisional torques have been computed by ASCOT in full 3D geometry in both the axisymmetric and perturbed equilibrium, which includes the B-coil perturbation. Note that the torque due to the interaction between the fast-ions and the MP field is contained in the fast-ion $j \times B$ driven torque.

Although the impact of fast-ion non-ambipolar transport on the bulk plasma is very complex, we can qualitatively interpret the observed change of toroidal rotation in terms of momentum conservation by using the following simple model. We have estimated the steady state toroidal rotation (v_ϕ) by means of equation (75) in [56]:

$$v_\phi = \frac{T_\phi}{m_{eff} n_e R} \tau_\phi \tag{2}$$

Here T_ϕ is the input beam torque as computed by ASCOT, τ_ϕ the momentum confinement time calculated by TRANSP, R the flux surface average major radius and m_{eff} is the effective mass defined as $m_{eff} = (m_D n_D + m_{imp} n_{imp}) n_e^{-1}$, where n_{imp} and m_{imp} are the impurity density and mass. The effective charge is set to 1.5 to calculate the input main ion and impurity density profiles provided for the simulations from the electron density profile using quasi-neutrality. The electron density profiles at $t = 4.45$ s and $t = 4.75$ s have been used to take into account the observed density pump-out. The volume integration has been considered. According to TRANSP, the momentum confinement time during the application of MPs is reduced by approximately 10-15% and 30-35% in discharges #28059 and #28061, respectively, compared to the axisymmetric reference. Note that this is due to the density pump-out and change in co-I_p toroidal rotation induced by the perturbation field, as TRANSP does not include 3D magnetic field geometry in the input torque calculation. This reduction of the momentum confinement time is related to the degradation of particle transport (relative change of density profile, or density pump-out, in the pedestal region of 10 and 25%, respectively, as reported in section 2.2).

We focus the analysis on the third phase, in which the radial beams #3 and #5 are used, which inject mostly trapped particles. Figures 11(a,e) show the $j \times B$ ($T_{j\times B}$) and collisional (T_{coll}) torques for discharges #28059 and #28061 as calculated by ASCOT for the axisymmetric equilibrium in black (t = 4.45 s) and perturbed equilibrium (t = 4.75 s) in red (vacuum) and blue (including the plasma response). It is interesting to note that the plasma response shields the impact of the field perturbation on $T_{j\times B}$ for the high q_{95} case, such that the plasma response torque lies between the axisymmetric and the vacuum calculations, i.e. $T_{j\times B}$ calculated including plasma response (blue) lies between the vacuum calculation (red) and the axisymmetric case (black), as shown in figure 11(a). On the contrary, in the low q_{95} case the plasma response enhances $T_{j\times B}$ at the edge (blue), such that it becomes more counter-current compared to the vacuum calculation (red) and underlines the differences with the axisymmetric torque (black), as shown in figure 11(e). These simulations support the idea that the reduction of the co-I_p rotation is due to an increase in counter-I_p torque from the fast-ion $T_{j\times B}$, rather than a rotation braking/dissipation.

Deep in the plasma core (highlighted in blue in figures 11(a)-(f)), the small plasma volume gives rise to poor statistics in the torque calculation. This region is, therefore, excluded from the analysis.

Figure 11(c,g) show the steady state toroidal rotation as calculated with equation 2 using $T = T_{coll} + T_{j\times B}$ (dashed lines) in the axisymmetric (black) and perturbed vacuum (red) and plasma response (blue) cases, as well as the experimental rotation profiles (squares). It can be seen that for the high q_{95} case the estimated toroidal rotation profile is overall unaffected up to the pedestal top by the MPs, while for the low q_{95} experimental toroidal rotation reduction is qualitatively reproduced across the full plasma radius. Figures 11(d,h) show the variation of toroidal rotation ($\Delta v_\phi = v_{\phi,MP} - v_{\phi,axis}$) in the experiment (squares) and the simulated one using vacuum (dashed red lines) and plasma response (dashed blue lines) approximation using $T = T_{coll} + T_{j\times B}$. The simple model captures the reduction of co-I_p rotation in excellent agreement with the experiment for the low q_{95} case, as shown in figure 11(h) across the full plasma radius. For the high q_{95} case, the agreement is good from mid-radius up to the pedestal top. It is interesting to highlight that including plasma response improves agreement between experiment and simulation across the full

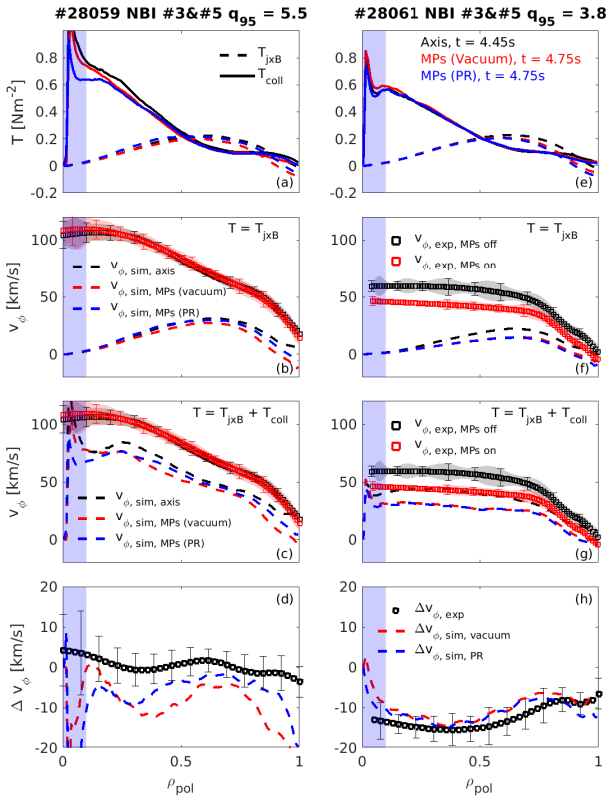

Figure 11. Simulated torques and experimental and estimated v_ϕ profiles for the low (left, a-d) and high (right, e-h) q_{95} discharges are shown. (a,e) Beam driven $j \times B$ (solid) and collisional (dashed) torques as calculated by ASCOT. (b,f) The toroidal rotation as calculated by equation 2 using $T = T_{j\times B}$ (solid) and the experimental profiles (squares) with error-bars. (c,g) The toroidal rotation as calculated by equation 2 using $T = T_{j\times B} + T_{coll}$ (solid) and the experimental profiles (squares) with error-bars. Colour code applies to both simulation and measurements and corresponds to the axisymmetric case (black), vacuum perturbed field (red) and plasma response fields (blue). (d,h) The experimental (squares) and simulated (dashed lines, red and blue for vacuum and plasma response, respectively) variation of toroidal rotation with respect to the axisymmetric case.

plasma radius, and especially in the pedestal top region ($\rho_{pol} = [0.8, 0.9]$). This suggests that for the high q_{95} case a stronger shielding of the perturbation field would be required to match the experimental observation [41].

Figure 11(b,f) show the steady state toroidal rotation as calculated with equation 2 assuming $T = T_{j\times B}$. When comparing the two discharges, we observe that the perturbation results in a smaller co-I_p rotation that is limited to the pedestal region in the high q_{95}, while in the low q_{95} the impact of the changes in the input torque on the rotation profile penetrate further inwards. The simple model qualitatively reproduces the co-I_p rotation reduction at the plasma edge within an order of magnitude taking into account only the changes in the fast-ion $T_{j\times B}$ for the low q_{95} discharge. However, it overestimates the co-I_p toroidal rotation reduction for the high q_{95} discharge, as some level of counter-I_p v_ϕ is predicted and in the experiment the rotation profile remains mostly unaffected. Deeper inside the plasma, the calculated rotation profiles overlap in both discharges and are far from the experimental value. The agreement of the calculated v_ϕ with the experimental values improves, especially in the plasma core, when including the collisional torque in the calculation (using equation 2 and $T = T_{coll} + T_{j\times B}$), as shown in figures 11(c,g). This is consistent with the $j \times B$ torque being an important contribution at the plasma edge while in the plasma core T_{coll} plays a more important role.

For the second phase (tangential beam), the model captures the qualitative change in the toroidal rotation profile, although it underpredicts the co-I_p toroidal rotation reduction for the low q_{95} case in a factor of 2. For the high q_{95} case, the model is able to reproduce adequately the absence of a change in the toroidal rotation profile for the second phase (there is some disagreement at the very edge, as for the third phase). The model can reproduce the experimental observation in the first phase with high accuracy for $\rho_{pol} > 0.4$ in the high q_{95} case.

This simple model is therefore able to capture generally the experimental observations and the two cases shown in figure 11 are representative of the three phases. It is important to note that both the changes in the fast-ion driven torques and the changes in the confinement are important for reproducing the changes observed in the experimental toroidal rotation profiles. It is important to highlight that in these calculations, the effects of MPs on the different transport channels have been included by using the experimental density profile, the torque profiles as calculated by ASCOT and the momentum confinement time as calculated by TRANSP to assess their impact on the toroidal rotation profile. If the momentum confinement time (τ_ϕ) is kept fixed to the unperturbed (axisymmetric value), the change of the beam driven torques is sufficient to describe the reduction of the co-I_p rotation at the plasma edge. However, the use of the corresponding τ_ϕ profile as estimated by TRANSP for both the MPs on and off phases, is important to also reproduce the reduction of co-I_p rotation in the plasma core.

The approximation of impurity toroidal rotation being the bulk plasma toroidal rotation has been made, however the changes in impurity flows might not be representative of changes in main ion flows at the plasma edge depending on plasma collisionality [57]. The response of main ion toroidal rotation [58–60] to symmetry breaking 3D fields, which represents the true bulk plasma rotation, is subject of future work.

Although momentum balance is a complex

problem and many terms enter the momentum balance equation, by means of this simplified model the impact of fast-ion transport on the toroidal rotation can be estimated. A discussion of other momentum driving and damping mechanisms that can have an effect on the toroidal rotation profile is given in the next subsection.

6.1. Discussion on other damping and driving momentum mechanisms

This work focuses on the impact of symmetry breaking fields on fast-ion driven torques and their subsequent impact on plasma toroidal rotation. There are other momentum damping and driving mechanisms which can influence the toroidal rotation profile that have not been included. Amongst other possible contributors are resonant and thermal NTV torques [12, 41, 46], changes in turbulence [46] and intrinsic rotation driven torques [61–65], friction with neutrals at the plasma edge [66,67] and ambipolarity restoring torques [67–70] due to edge stochastization [71]. [72] studied the resonant and thermal NTV torque in the low q_{95} discharge, and showed that the thermal NTV torque is negligible for this case. Note that the study presented in [72] relied on beam torque calculations from TRANSP (in a 2D equilibrium, which does not include the impact of the perturbation on non-ambipolar fast-ion transport), and the resonant torques were adjusted manually to match the experimental rotation braking. In [46] it was shown that the Reynold stress driven torque for a low q_{95} discharge is an order of magnitude smaller than the thermal NTV and $j \times B$ torques. The changes of the NBI driven torque due to the MPs calculated in this work are comparable to the thermal NTV and resonant torques reported in [46]. . The neutral torque has been estimated with TRANSP and shows a negligible effect on the calculated toroidal rotation for this discharge (of 0.04 km/s at $\rho_{pol} = 0.95$, being the change in neutral torque at this location 0.3% of the change in the beam torque). Thus, it has been neglected in the analysis. In addition, the spin up of the edge toroidal rotation in the co-I_p direction, due to the edge stochastization, is the opposite phenomenom observed in the low collisionality H-mode discharges analyzed in this work.

7. Conclusions and outlook

This work characterizes the impact that external magnetic perturbations have on the coupled temporal evolution of fast-ion losses and toroidal rotation in a low and high q_{95} discharge of ASDEX Upgrade. An analysis technique has been developed, based on correlation calculations, which allows us to shed light on the relations between the variables of interest, as it enables us to identify their interdependencies as a function of the radius and the fast-ion energy and pitch angle. From the correlation analysis we can extract that the correlation intensifies towards the plasma edge, suggesting that the lost fast-ions can have a stronger impact on rotation in this region. The observation of an abrupt change in the correlation due to a variation in pitch angle is in line with fast-ion transport due to MPs being resonant and thus, strongly dependent on the ion orbit topology. These results agree with the existence of an Edge Resonant Transport Layer (ERTL) [22] in the presence of 3D perturbative fields.

Orbit following ASCOT simulations, using both the vacuum and the plasma response approach, have been used to characterize the fast-ion transport predicted by the ERTL model. The impact of this transport on the $j \times B$ fast-ion torque, and the changes in the collisional torque deposition due to the density pump-out have been calculated. The impact of MPs on fast-ion and thermal plasma confinement have been related to the toroidal rotation changes via the momentum balance equation. The experimental toroidal rotation reduction has been qualitatively reproduced by means of a simple model and realistic torque calculations in full 3D magnetic field and wall geometry, with high accuracy for the low q_{95} discharge. The rotation braking is linked to a reduced co-I_p/increased counter-I_p fast-ion driven torque due to the radial transport of fast-ions induced by the external MP, rather than to a torque dissipation mechanism. For the high q_{95} case, the co-I_p rotation reduction is overpredicted in the pedestal region. This may be related to a stronger shielding of the perturbation by plasma response than the one estimated with VMEC. This result shows the importance of calculating beam driven torques in full 3D geometry when studying neoclassical toroidal viscous torques, and the need for accurate models for calculating plasma response.

The fast-ion resonant transport and the beam driven torques have been characterized in a high and low q_{95} discharge. The experimental differences observed between the high and the low q_{95} cases are connected to the shielding and amplification, respectively, of the external perturbation due to the plasma response.

While there is large evidence on the benefits of rotation for tokamak performance [73, 74], the direct NBI drive of rotation in future fusion devices, such as ITER, will be challenging. In ITER, NBI deposition will be more localized in the plasma edge compared to current tokamaks [75]. Considering the fast-ion driven transport due to symmetry breaking fields may be therefore important for predicting the NBI driven torque in future fusion devices. Since the

magnetic perturbations act differently on the multi-transport channels, the consideration of its impact on thermal plasma, NBI fast-ion and momentum transport channels will be key for effective application of MPs in future devices. The optimization of the MP configuration for NBI fast-ion transport control in ITER has been shown to be independent from ELM control capabilities [76]. This implies that the simultaneous optimization of thermal and NBI fast-ion transport in ITER is possible. The modelling tools presented in this work may enable to go one step further, and include the rotation drive as an additional parameter in the optimization of the MP used for ELM control in future fusion devices. This may also enable tailoring the torque profile by optimizing the chosen combination of the poloidal spectrum of the perturbation and q-profile, while good fast-ion transport is maintained. Finally, it is important to highlight that for such an optimization, the effects of plasma response are key, as the amplification and shielding of the perturbation fields, which also depend on q_{95} and the poloidal spectrum of the perturbation, are crucial for the accurate prediction of the impact of MPs on the plasma performance.

Acknowledgements

The authors would like to thank the referees for their valuable input. This work has received funding from the Spanish Ministry of Science, Innovation and Universities (grant FPU17/06273), the H2020 Marie-Sklodowska Curie programme (grant No. 708257) and the European Research Council (ERC) under the European Union's Horizon 2020 research and innovation programme (grant agreement No 805162). The simulations were partly performed on the MARCONI supercomputer (CINECA) under project reference FUA33_ASCOT-US. This work has been partially carried out within the framework of the EUROfusion Consortium and has partially received funding from the Euratom research and training programme 2014-2018 and 2019-2020 under grant agreement No 633053. The views and opinions expressed herein do not necessarily reflect those of the European Commission.

References

[1] TC Hender *et al*. *Nucl. Fusion*, 32(2091), 1992.
[2] TE Evans *et al*. *Phys. Rev. Lett.*, 92(235003), 2004.
[3] Y Liang *et al*. *Phys. Rev. Lett.*, 98(265004), 2007.
[4] W Suttrop *et al*. *Phys. Rev. Lett.*, 106(225004), 2011.
[5] KC Shaing and DJ Callen. *Phys. of Fluids*, 26(3315), 1983.
[6] JK Park *et al*. *Phys. Rev. Lett.*, 102:065002, 2009.
[7] AH Boozer. *Phys. Fluids*, 19(149), 1976.
[8] AH Boozer. *Phys. Fluids*, 23(2283), 1980.
[9] AH Boozer. *Phys. Rev. Lett.*, 86(2), 2001.
[10] Y Sun *et al*. *Phys. Rev. Lett.*, 105(145002), 2010.
[11] W Zhu *et al*. *Phys. Rev. Lett.*, 96(225002), 2006.
[12] AM Garofalo *et al*. *Phys. Rev. Lett.*, 101(195005), 2008.
[13] KC Shaing. *Phys. Plasmas*, 10,(1443), 2003.
[14] KC Shaing *et al*. *Phys. Plasmas*, 15,(082506), 2008.
[15] K Kim *et al*. *Phys. Plasmas*, 19(082503), 2012.
[16] K Kim *et al*. *Phys. Rev. Lett.*, 110(185004), 2013.
[17] WW Heidbrink *et al*. *Phys. Plasmas*, 15(055501), 2008.
[18] M Garcia-Munoz *et al*. *Nucl. Fusion*, 53(123008), 2013.
[19] M Garcia-Munoz *et al*. *Plasma Phys. and Control. Fusion*, 55(124014), 2013.
[20] T Kurki-Suonio *et al*. *Plasma Phys. Control. Fusion*, 59(014013), 2017.
[21] K Shinohara *et al*. *Nucl. Fusion*, 51:63028, 2011.
[22] L Sanchis *et al*. *Plasma Phys. Control. Fusion*, 61:014038, 2019.
[23] U Stroth *et al*. *Plasma Phys. Control. Fusion*, 53(024006), 2011.
[24] XD Du *et al*. *Nucl. Fusion*, 56(016002), 2016.
[25] WW Heidbrink *et al*. *Plasma Phys. Control. Fusion*, 53(085028), 2011.
[26] E Strumberger *et al*. *Nucl. Fusion*, 54(064019), 2014.
[27] W Suttrop *et al*. *Fusion Eng. Des.*, 84(290-294):2–6, 2009.
[28] M Garcia-Munoz *et al*. *Rev. Sci. Instrum*, 80(053503), 2009.
[29] PA Schneider *et al*. *Plasma Phys. and Control. Fusion*, 54(105009), 2012.
[30] R Fischer *et al*. *Fusion Sci. Technol.*, 58(675), 2010.
[31] E Viezzer *et al*. *Rev. Sci. Instrum.*, 83(103501), 2012.
[32] RM McDermott *et al*. *Rev. Sci. Instrum.*, 88(073508), 2017.
[33] B Kurzan *et al*. *Rev. Sci. Instrum.*, 82(103501), 2011.
[34] M Willensdorfer *et al*. *Rev. Sci. Instrum.*, 83(023501), 2012.
[35] C Paz-Soldan *et al*. *Phys. Rev. Lett.*, 114(105001), 2015.
[36] A Kirk *et al*. *Nucl. Fusion*, 55(043011), 2015.
[37] A Kirk *et al*. *Nucl. Fusion*, 53(043007), 2013.
[38] MW Jakubowski *et al*. *Influence of Magnetic Perturbations on Particle Transport in magnetic fusion devices*. St Petersburg, 2014. EX/P3-47, paper presented at 25^{th} IAEA Int. Conf. on Fusion Energy.
[39] E Viezzer *et al*. *Nucl. Fusion*, 53(053005), 2013.
[40] GD Conway *et al*. *Plasma Phys. Control. Fusion*, 57(014035), 2015.
[41] W Suttrop *et al*. *Plasma Phys. Control. Fusion*, 59(014049), 2017.
[42] N Leuthold *et al*. *Plasma Phys. Control. Fusion*, 59(055004), 2017.
[43] E Viezzer *et al*. *Nucl. Fusion*, 53(123002), 2015.
[44] Y Liu *et al*. *Phys. Plasmas*, 17(122502), 2010.
[45] Y Liu *et al*. *Nucl. Fusion*, 51(083002), 2011.
[46] Y Liu *et al*. *Nucl. Fusion*, 56(056015), 2016.
[47] AD Turnbull. *Nucl. Fusion*, 52(054016), 2012.
[48] A Wingen *et al*. *Phys. Plasmas*, 18(042501), 2011.
[49] M Bécoulet *et al*. *Nucl. Fusion*, 52(054003), 2012.
[50] DA Ryan *et al*. *Plasma Phys. Control. Fusion*, 57(095008), 2015.
[51] MJ Lanctot *et al*. *Nucl. Fusion*, 53(083019), 2013.
[52] F Orain *et al*. *Nucl. Fusion*, 57(022013), 2017.
[53] FD Schönbrodt and M Perugini. *Journal of Research in Personality*, 47:609–612, 2013.
[54] K Kim *et al*. *Phys. Plasmas 25*, 25(122511), 2018.
[55] E Hirvijoki *et al*. *Comput. Phys. Commun.*, 185(1310), 2014.
[56] FL Hinton and MN Rosenbluth. *Physics Letters A*, 259:267–275, 1999.
[57] FL Hinton and RD Hazeltine. *Rev. Mod. Physics*, 48(239), 1976.
[58] B. Grierson *et al*. *Rev. Sci. Instrum*, 83(10D529), 2012.
[59] S.R. Haskey *et al*. *Rev. Sci. Instrum*, 89(10D110), 2018.

[60] P Cano-Megias *et al*. *JINST*, 14(C10040), 2019.
[61] T Stoltzfus-Dueck. *Plasma Phys. Control. Fusion*, 61(124003), 2019.
[62] J Omotani *et al*. *Nucl. Fusion*, 56(124002), 2016.
[63] WM Solomon *et al*. *Phys. Plasmas*, 17(056108), 2010.
[64] RM McDermott *et al*. *Nucl. Fusion*, 54(043009), 2014.
[65] C Angioni *et al*. *Phys. Rev. Lett.*, 107(215003), 2011.
[66] J Omotani *et al*. *Journal of Physics*, 775(012011), 2016.
[67] L Piron *et al*. *Nucl. Fusion*, 53(113002), 2013.
[68] JW Coenen *et al*. *Nucl. Fusion*, 51(063030), 2011.
[69] S Mordijck *et al*. *Nucl. Fusion*, 54:082003, 2014.
[70] L Schmitz *et al*. *Nucl. Fusion*, 59:126010, 2019.
[71] E Kaveeva, V Rozhansky and M Tendler. *Nucl. Fusion*, 48:075003, 2008.
[72] S Fietz *et al*. *Nucl. Fusion*, 55(013018), 2015.
[73] JE Rice. *Plasma Phys. Control. Fusion*, 58(083001), 2016.
[74] K Ida and JE Rice. *Nucl. Fusion*, 54(045001):29, 2014.
[75] C Hopf *et al*. *Nucl. Fusion*, 61(106032), 2021.
[76] L Sanchis *et al*. *Nucl. Fusion*, 61(046006), 2021.